PREPARATION AND TESTING OF CORROSION- AND SPALLATION-RESISTANT COATINGS

Annual Topical Report

Reporting Period Start Date: October 1, 2011
Reporting Period End Date: September 30, 2012

Project Reporting Period: October 1, 2011 – September 30, 2013

Principal Author: John P. Hurley

Report Issue Date: October 2012
DOE NETL Cooperative Agreement DE-FE0007325
Performance Monitor: Briggs White

Submitting Organization:

Energy & Environmental Research Center
15 North 23rd Street, Stop 9018
Grand Forks, ND 58202-9018

John P. Hurley, Project Manager

October 2012

DISCLAIMER

This report was prepared as an account of work sponsored by an agency of the United States Government. Neither the United States Government, nor any agency thereof, nor any of their employees, makes any warranty, express or implied, or assumes any legal liability or responsibility for the accuracy, completeness, or usefulness of any information, apparatus, product, or process disclosed, or represents that its use would not infringe privately owned rights. Reference herein to any specific commercial product, process, or service by trade name, trademark, manufacturer, or otherwise does not necessarily constitute or imply its endorsement, recommendation, or favoring by the United States Government or any agency thereof. The views and opinions of authors expressed herein do not necessarily state or reflect those of the United States Government or any agency thereof.

PREPARATION AND TESTING OF CORROSION- AND SPALLATION-RESISTANT COATINGS

ABSTRACT

This Energy & Environmental Research Center (EERC) project is designed to determine if plating APMT, a specific highly oxidation-resistant oxide dispersion-strengthened FeCrAl alloy made by Kanthal, onto nickel-based superalloy turbine parts is a viable method for substantially improving the lifetimes and maximum use temperatures of the parts. The method for joining the APMT plate to the superalloys is called evaporative metal bonding. It involves placing a thin foil of zinc (Zn) between the plate and the superalloy, clamping them together, and heating in an atmosphere-controlled furnace. Upon heating, the Zn melts and dissolves the oxide skins of the alloys at the bond line, allowing the two alloys to diffuse into each other. The Zn then diffuses through the alloys and evaporates from their surfaces.

Laboratory testing has shown that the diffusion rate of Zn through the FeCrAl alloy is much faster than through the nickel superalloys. This means that the FeCrAl will serve as a sink for the Zn bonding alloy during the evaporative metal bonding process. Also, the testing has shown that the Zn diffusion mechanism is bulk diffusion, and not intergranular. This is a surprise. However, it means that quantification of the Zn diffusivities in these samples will be significantly simpler than would have been the case if grain boundary diffusion dominated.

In addition to the laboratory testing, gas impinger and particulate samples are being collected from a combustor firing syngas and natural gas to determine what types of microcontaminants may reach a turbine firing syngas. The syngas is created in one of two different pilot-scale pressurized coal gasifiers. The initial analysis of the impinger solutions was for standard U.S. Environmental Protection Agency (EPA) Method 29 determination of hazardous metals and did not include major element analysis. When syngas is fired, the amount of Mn in the combustor gas increases substantially. Halogens (Br_2 and Cl_2) and hydrogen halides (HF, HCl, and HBr) are present in amounts close to or below 1 ppm. In the near future, the solutions will be reanalyzed for major elements.

SEM analysis showed that the particulate matter is primarily nonstoichiometric iron sulfate. Most of the particles were 3 µm in diameter or less. Elements such as O, Fe, S, Cr, and Si make up the majority of the compositions of 3089 particles analyzed on the filter surface. The concentrations of O and S are high in almost all particles. The concentrations of S and Fe tend to be higher in the larger particles than in the smaller. In contrast the concentrations of O showed the reverse trend. We currently believe that the high values of Fe and Cr come from a reaction of the syngas with the stainless steel pipes used to transport the syngas, most likely by forming a vapor-phase carbonyl. During combustion, the carbonyls form nonstoichiometric sulfate particles. The excess Si is most likely coming from the coal ash, possibly through the formation of a silicon monoxide fume.

TABLE OF CONTENTS

LIST OF FIGURES ii

LIST OF TABLES iii

NONMENCLATURE iv

EXECUTIVE SUMMARY v

INTRODUCTION 1

EXPERIMENTAL METHODS 1
- Laboratory Testing and Modeling 1
- Gasifier Sampling 3

RESULTS AND DISCUSSION 11
- Laboratory Testing and Modeling 11
- Gasifier Sampling 15
  - Impinger Solution Analyses 15
  - SEM Analysis of a Filter Sample 19

CONCLUSIONS 23

LIST OF FIGURES

1 a) assembled bonding jig and sample and b) separate bonding components 2

2 Pressure-sensitive film showing the need for additional polishing after initial sample machining 3

3 EFG 4

4 The EFG equipment used to produce the syngas sampled during this reporting period..... 5

5 Design drawing of the pressurized fluidized-bed gasification reactor 6

6 Photograph of the high-pressure FBG 7

7 Cross-sectional view of the fuel feed system 7

8 Photograph of the fluid-bed coal feed system 8

9 M29 and 26A sampling train 10

10 Elemental map of Zn – CM247LC bonded at 1214°C for 1 hour: a) joint edge and b) joint center 12

11 Elemental map of Zn – CM247LC bonded at 1214°C for 3 hours 13

12 Elemental map of Zn – Rene 80 bonded at 1214°C for 1 hour 13

13 Elemental map of Zn – APMT bonded at 1214°C (joint center) for a) 1 hour and b) 3 hours 14

14 Comparison of strains in the bonding assembly when loads applied at a) joint center or b) joint ends 16

15 Desiccator containing collected filter samples 19

16 SEM images of the filter particles obtained at different magnifications 20

17 Particles chosen for full spectral analysis 20

18 Cumulative size distribution of the 3089 particles analyzed 21

19 Composition vs. size of particles 22

20 Composition vs. shape of particles 22

LIST OF TABLES

1 Limit of Detection of Trace Metals Analyzed 11

2 M29 Results, Test 2, March 28, 2012 17

3 M29 Results, Test 3, March 30, 2012 17

4 M29 Results, Test 4, April 11, 2012 18

5 M26A Results, Test 5, April 11, 2012 18

6 M26A Results, Test 6, April 18, 2012 19

7 Elemental Compositions of the Five Particles Chosen 21

8 Composition of 316L Stainless Steel 23

NONMENCLATURE

APMT	oxide dispersion-strengthened FeCrAl alloy made by Kanthal
ASME	American Society of Mechanical Engineers
CM247LC	alumina-scale-forming nickel-based superalloy
CVAAS	cold-vapor atomic absorption spectrometry
EDM	electrical discharge machining
EDS	energy-dispersive spectroscopy
EFG	entrained-flow gasifier
EMB	evaporative metal bonding
EPA	U.S. Environmental Protection Agency
FBG	fluidized-bed gasifier
HGFV	hot-gas filter vessel
HHC	higher hydrogen content
IC	ion chromatography
ICP	inductively coupled plasma
LLQ	lower limit of quantification
MS	mass spectrometry
Rene80	alumina-scale-forming nickel-based superalloy
SEM	scanning electron microscopy

PREPARATION AND TESTING OF CORROSION- AND SPALLATION-RESISTANT COATINGS

EXECUTIVE SUMMARY

This Energy & Environmental Research Center project was designed to determine if plating APMT, a specific highly oxidation-resistant oxide dispersion-strengthened FeCrAl alloy made by Kanthal, onto nickel-based superalloy turbine parts is a viable method for substantially improving the lifetimes and maximum use temperatures of the parts, both those with thermal barrier coatings and those without. The superalloys being investigated for protection are CM247LC and Rene 80. Both are alumina-scale-forming alloys. The method for bonding the APMT plate to the superalloys is called evaporative metal bonding, which involves placing a thin foil of zinc (Zn) between the plate and the superalloy, clamping them together, and heating in an atmosphere-controlled furnace. Upon heating, the Zn melts and dissolves the oxide skins of the alloys at the bond line, allowing the two alloys to diffuse into each other. The Zn then diffuses through the alloys and evaporates from their surfaces.

If successful, the information developed will help move the protection process closer to demonstration testing. In addition, the team will characterize the microcontaminants in combusted higher-hydrogen-content gas. This information will be used to best simulate actual corrosion conditions in a turbine system and can also be used by other researchers studying deposition and gas flow in turbines.

Laboratory testing has shown that the diffusion rate of Zn through the FeCrAl alloy is much faster than through the nickel superalloys. This means that the FeCrAl will serve as a sink for the Zn bonding metal during the evaporative metal bonding process. Also, the testing has shown that the Zn diffusion mechanism is bulk diffusion, and not intergranular. This is a surprise. However, it means that quantification of the Zn diffusivities in these samples will be significantly simpler than would have been the case if grain boundary diffusion dominated. Quantitative zinc diffusion profiles are currently being generated for the samples so that diffusivities can be calculated and the complete history of the Zn from bonding foil to diffusion through the alloys to evaporation can be understood.

In addition to the laboratory testing, gas impinger and particulate samples are being collected from a combustor firing syngas and natural gas to determine what type of microcontaminants may reach a turbine system firing syngas. The syngas is created in one of two different pilot-scale pressurized gasifiers. The initial analysis of the impinger solutions was for standard U.S. Environmental Protection Agency (EPA) Method (M) 29 determination of hazardous metals. The data show that when only natural gas is fired in the combustor, all of the hazardous elements analyzed for the M29 test matrix except As and Co are present at low levels in the gas collected from the thermal oxidizer. It is not yet known if the metals come into the thermal oxidizer in the natural gas or air or, more likely, are contaminants previously deposited in the thermal oxidizer. However, when syngas is fired, the amount of Mn in the gas stream increases substantially. Ion chromatography (IC) results show that halogens (Br_2 and Cl_2) and hydrogen halides (HF, HCl and HBr) are present in amounts close to or below their respective

lower levels of quantification of 1 ppm. In the near future, more M26A samples will be collected during entrained-flow gasifier (EFG) testing to determine if their levels remain as low as for the fluid-bed gasifier (FBG) samples. In addition, the solutions will be reanalyzed for major elements.

SEM analysis showed that the particulate matter is primarily nonstoichiometric iron sulfate. Most of the particles were 3 µm in diameter or less. Elements such as O, Fe, S, Cr, Si, and traces of Na, Ni, Al, Mg, K, Ca, and Mn were detected in the 3089 particles analyzed on the filter surface. The concentrations of O and S are high in almost all particles. The data show that the concentrations of S and Fe tend to be higher in the larger particles than in the smaller. In contrast, the concentrations of O showed the reverse trend. The average shape factor of most particles was about 1.2, meaning that most of them have a nearly spherical shape.

We currently believe that the high values of Fe and Cr observed on the filter samples come from a reaction of the syngas with the stainless steel pipes used to transport the syngas, most likely by forming vapor-phase carbonyls. During combustion of the carbonyls in the thermal oxidizer, they react to form nonstoichiometric sulfate particles. The excess Si is most likely coming from the coal ash, possibly through the formation of a silicon monoxide fume. In the thermal oxidizer, the silicon monoxide may oxidize to form a small particle of silicon dioxide, which may then serve as a nucleation site for the iron-rich sulfate.

PREPARATION AND TESTING OF CORROSION- AND SPALLATION-RESISTANT COATINGS

INTRODUCTION

The objective of this Energy & Environmental Research Center (EERC) was to take a recently developed method of plating nickel superalloys with protective FeCrAl layers closer to commercial use in syngas-fired turbines. The project is designed to determine if plating APMT, a specific highly oxidation-resistant oxide dispersion-strengthened FeCrAl alloy made by Kanthal, onto nickel-based superalloy turbine parts is a viable method for substantially improving the lifetimes and maximum use temperatures of the parts, both those with thermal barrier coatings (TBCs) and those without. The superalloys being investigated for protection are CM247LC and Rene 80. Both are alumina-scale-forming alloys. The method for bonding the APMT plate to the superalloys is called evaporative metal bonding (EMB), which involves placing a thin foil of zinc (Zn) between the plate and the superalloy, clamping them together, and heating in an atmosphere-controlled furnace. Upon heating, the Zn melts and dissolves the oxide skins of the alloys at the bond line, allowing the two alloys to diffuse into each other. The Zn then diffuses through the alloys and evaporates from their surfaces.

If successful, the information developed will help move the protection process closer to demonstration testing. In addition, the team will characterize the microcontaminants in combusted higher-hydrogen-content (HHC) gas. This information will be used to best simulate actual corrosion conditions in a turbine system and can also be used by other researchers studying deposition and gas flow in turbines.

EXPERIMENTAL METHODS

Laboratory Testing and Modeling

Under Tasks 2 and 3, we are measuring properties of the alloys and developing computer models of their high-temperature properties in order to develop the best methods for joining the APMT plate to CM247LC and Rene 80 turbine parts. In order to determine the best heating schedules to use for joining APMT plates to superalloy parts, we are measuring the diffusion rates of Zn through the alloys as functions of temperature. In order to develop the best clamp designs to use for holding the plating to the parts, we are measuring physical properties of the materials as a function of temperature.

Over the last year, the first Zn diffusion samples were fabricated. Figure 1 shows a) the assembled bonding jig and sample and b) the separate bonding components. The jig assembly (body plus bolt) is fabricated from a magnesium alloy for its low thermal expansion.

Spherical steel (E52100) end caps to help with alignment of the bonding sample by allowing it to articulate to make sure that the clamping force is evenly distributed across the joint between the two alloy cylinders.

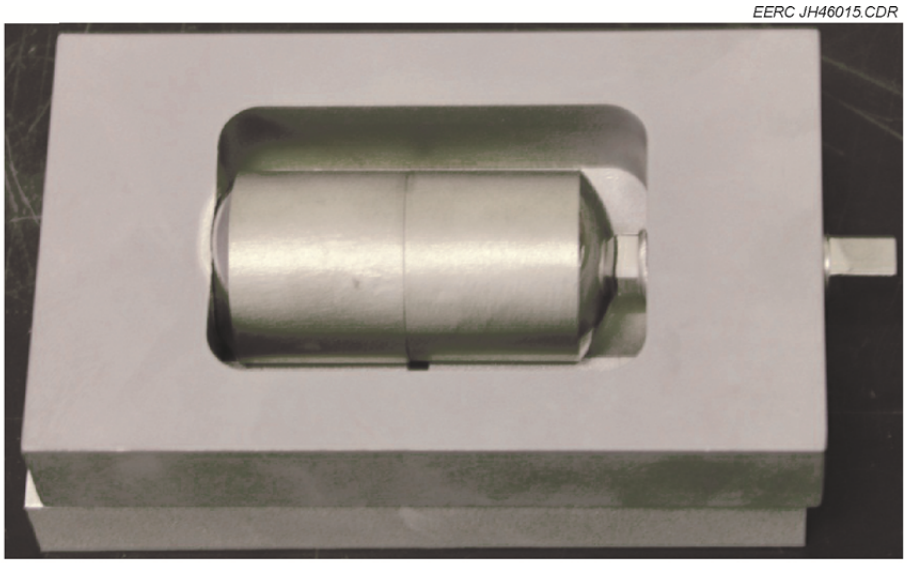

(a)

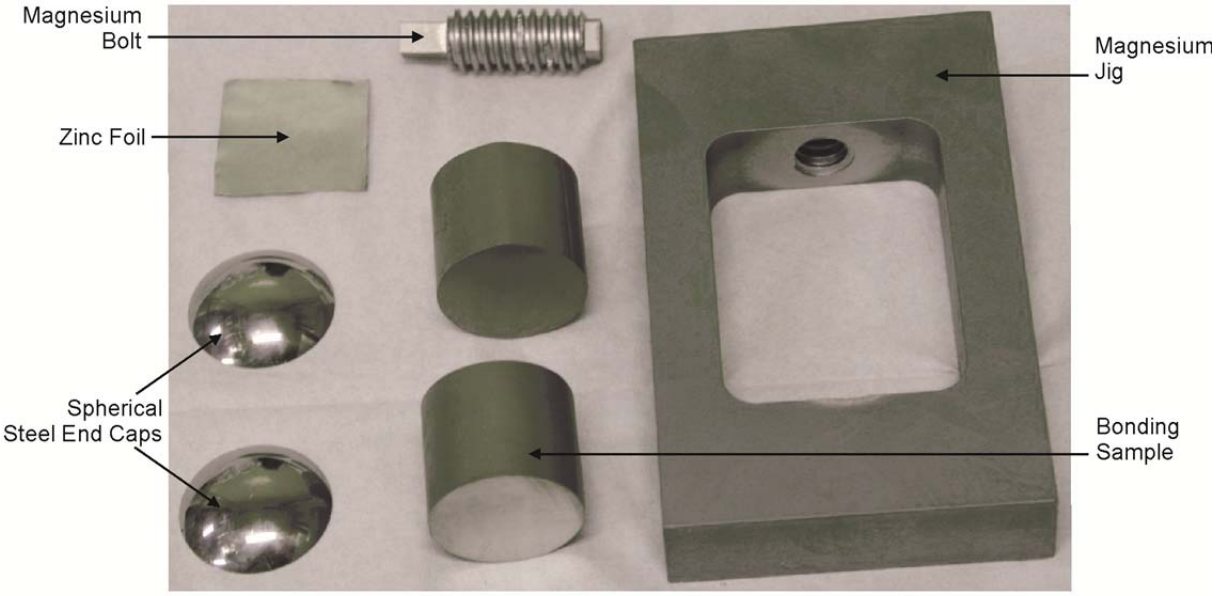

(b)

Figure 1. a) assembled bonding jig and sample and b) separate bonding components.

The diffusion bonding was achieved using the following process:

1) Bonding samples cut from larger rods using electrical discharge machining (EDM)
2) Bonding surfaces polished to 180 grit
3) Entire surface of bonding samples sandblasted
4) Bonding surfaces polished to 220 grit
5) Bonding samples, end caps, bolt, and jig ultrasonically cleaned in acetone
6) Bonding samples, end caps, bolt, and jig cleaned in isopropanol

Steps 2 and 4 were found to be necessary because the pressure distribution across the bonding surface is not uniform when the bonding assembly used bonding samples that had just been EDMed. Figure 2 shows an image of pressure-sensitive film that was sandwiched between the bonding samples in the bonding assembly. The red area to one side of the image shows a higher concentration of pressure. Following the polishing steps, the pressure was seen to be more evenly distributed.

Gasifier Sampling

In addition to the laboratory testing, we have begun Task 4 sampling activities to determine what types of trace contaminants may occur in cleaned syngas that could lead to corrosion issues in turbines firing syngas. The EERC has several pilot-scale gasifiers that are continually used in a variety of test configurations. Funding for the actual operation of the gasifiers comes from other projects than this University Turbine Systems Research project. The trace contaminants are collected using standard U.S. Environmental protection Agency (EPA) sampling techniques after the syngas produced by the gasifiers is burned in refractory-lined thermal oxidizers. The sampling trains used are for EPA Method (M) 29 sampling for particulate- and vapor-phase metals and M26A for halogens. Sampling is conducted when either one of two pilot-scale gasifiers are being operated. One is a pressurized entrained-flow gasifier (EFG), and the other is a pressurized fluidized-bed gasifier (FBG).

Figure 3 shows a cross-sectional view of the EFG. The EFG is a dry-feed, downfired system. The reactor tube is vertically housed in a pressure vessel approximately 24 in. in diameter and 7 ft in length. The EFG fires nominally 8 lb/h of coal and produces up to 20 scfm of fuel gas. The maximum allowable working pressure is 300 psig. The reactor has the capability

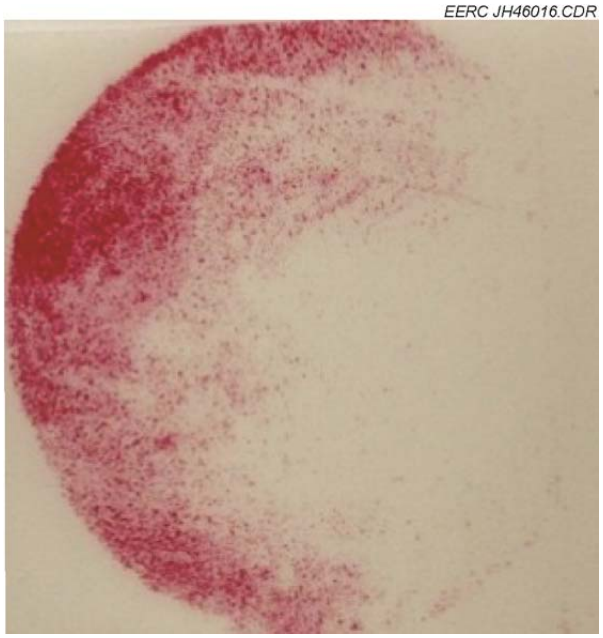

Figure 2. Pressure-sensitive film showing the need for additional polishing after initial sample machining.

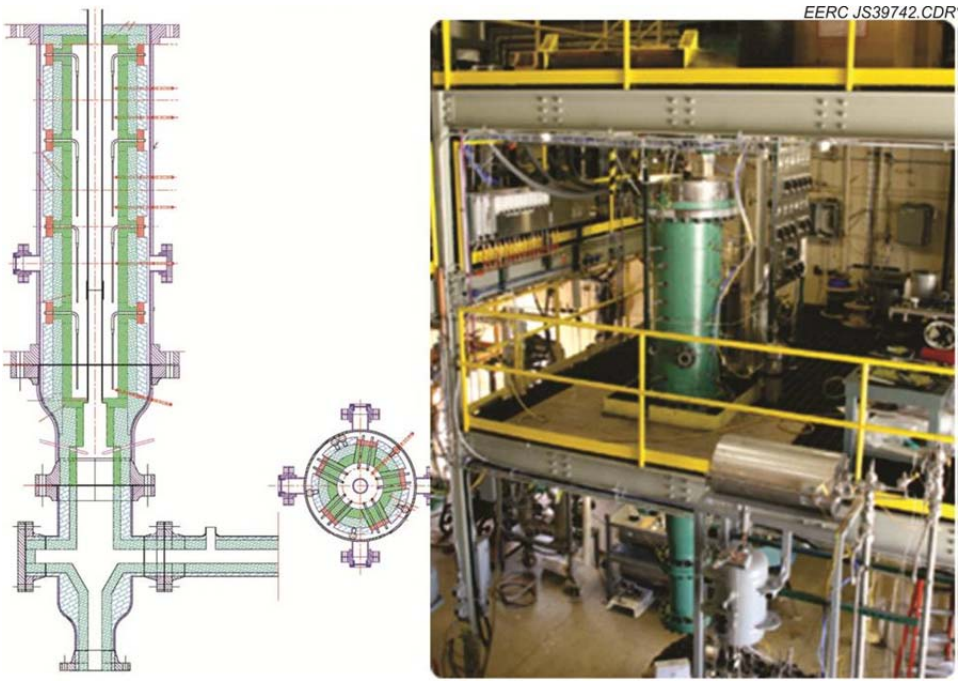

Figure 3. EFG.

to run in oxygen- or air-blown mode. The supplemental electrical heating system is capable of reaching a nominal temperature of 1500°C (2732°F) and is separated into four independent zones so that a consistent temperature can be maintained throughout the length of the furnace. The radially spaced heating elements provide the initial heat for the centrally located alumina reactor tube, and refractory walls outside the heating elements provide insulation. Type S thermocouples are used to monitor and control the temperatures of the heating zones and reactor tube. All of the gasification reactions occur inside the reactor tube, and slag is able to flow on the tube walls. Pressure inside the alumina reactor tube is balanced with a slightly positive nitrogen pressure outside of the alumina reactor tube.

Pulverized coal is fed into the top of the furnace via a twin-screw feeder and scale contained in a pressurized vessel. A lock hopper is in place that allows the system to be refilled while running, thereby facilitating continuous-mode operation. Feed rates are calculated in real time. The feed system can be run in either volumetric mode or gravimetric mode. Nitrogen or syngas is used to convey the solid pulverized coal into the combustion zone.

Product gas exits at the bottom of the furnace tube and enters a reducing section that houses a quench system capable of injecting water, syngas, or nitrogen as the quench fluid. The product gas then enters a cross, making a 90° turn, and then exits the main unit on its way to the back-end control devices. Slag, ash, and char drop through the cross and are collected in a refractory-lined slag trap. Fine particulate is able to flow with the gas through the 90° turn and is collected in a downstream filter.

The overall system layout for the test run is shown in Figure 4. Slag is collected below the gasifier in a refractory-lined slag trap. Fly ash is captured in the hot-gas filter vessel (HGFV) that uses an iron aluminide candle filter, providing near-absolute filtration. Dräger tube samples can be taken in the HGFV, measuring for ammonia, HCN, HCl, and H_2S. The gas then passes through water–gas shift reactors that can shift sour gas (containing H_2S) to increase its H_2 concentration. A portion then goes through sulfur adsorbers and then to hydrogen separation membranes that were tested during this run. The portion not going to the separation membranes is quenched to remove moisture and any tars formed in the system. All gas streams, including the membrane raffinate and permeate streams, are then recombined before combusting them in the thermal oxidizer from which the M29 samples are collected.

The pressurized FBG was designed according to American Society of Mechanical Engineers (ASME) B31.3 Process Piping Code specifications. After a review of available alloys, Haynes 556® was selected as the material most suitable for fabrication of this high-temperature, high-pressure system. The reactor was designed with the capability to operate at 6.9 MPa (1000 psig) at an operational temperature of 843°C (1550°F), 4.5 MPa (650 psig) at an operational temperature of 917°C (1650°F), and 2.0 MPa (300 psig) at an operational temperature of 1800°F. This system is externally electrically heated. Haynes 556 alloy was selected as the material of construction for the reactor, all the reactor nozzles, and the cyclone. A design drawing of the reactor is shown in Figure 5, and a photograph of the gasifier is shown in Figure 6. A design drawing of the fuel feed system is shown in Figure 7, with a photograph of the feeder vessel in Figure 8.

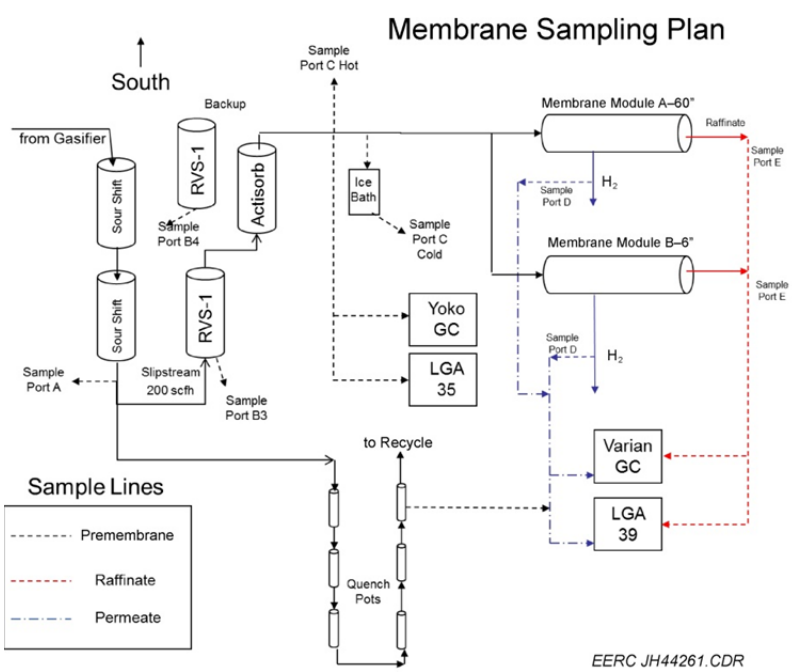

Figure 4. The EFG equipment used to produce the syngas sampled during this reporting period.

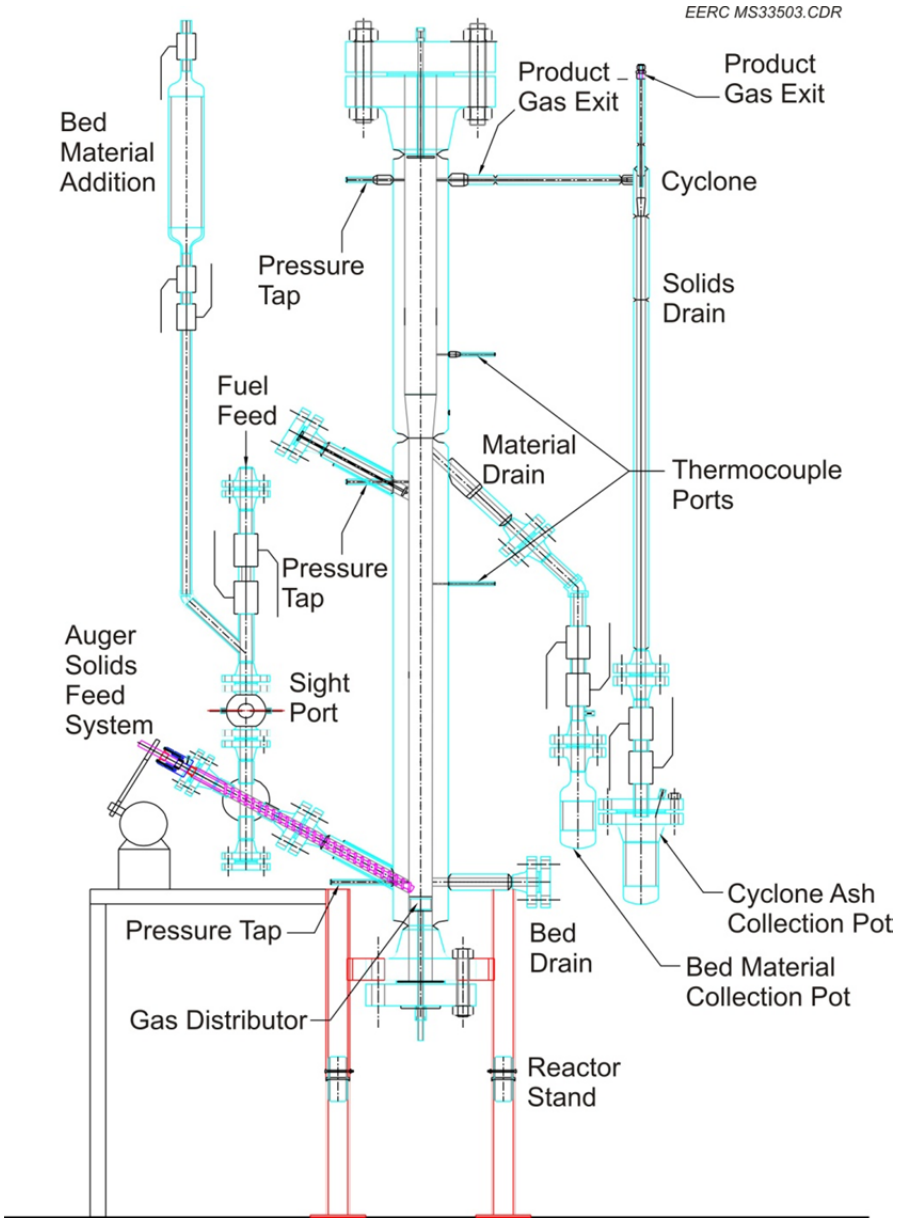

Figure 5. Design drawing of the pressurized fluidized-bed gasification reactor.

The FBG is capable of feeding up to 9.0 kg/hr (20 lb/hr) of pulverized coal or biomass at pressures up to 70 bar absolute (1000 psig). The externally heated bed is initially charged from an independent hopper with silica sand, but through time the bed converts to coal ash. Independent mass flow controllers meter the flow of nitrogen, oxygen, steam, and recycled syngas into the bottom of the fluid bed. Various safety interlocks prevent the inadvertent flow of pure oxygen into the bed or reverse flow into the coal feeder. Recycled syngas is injected several inches above the bottom distributor plate, which prevents direct combustion of syngas with oxygen entering at the bottom of the bed.

Figure 6. Photograph of the high-pressure FBG.

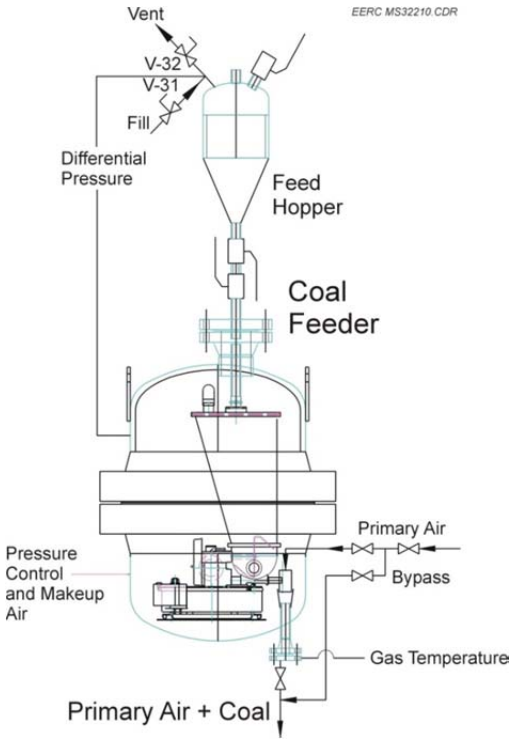

Figure 7. Cross-sectional view of the fuel feed system.

Figure 8. Photograph of the fluid-bed coal feed system.

The feed system uses a K-tron® loss-in-weight feeder setting inside of the pressure vessel capable of 6.9 MPa (1000 psig) operation. This system allows a real-time measurement of the fuel feed rate to the gasification system. The feed system electronic controls are interfaced to a data acquisition system that allows for local or remote computer control of the fuel feed rate. Power and electronic signals to and from the feeder are through two isolation fittings on the pressure vessel. The upper pressure vessel is the fuel charge hopper. The fuel charge hopper is manually charged with fuel through the top valve while at atmospheric pressure. It is then sealed and pressurized. Finally, the fuel feed material is transferred by gravity feed to the weigh hopper inside through the lower dual-valve system. The weigh hopper is on an integral platform scale that provides an electronic signal of the overall weight of the fuel feed material. Hopper weights along with feed rates are recorded by the data acquisition system and can be displayed and trended as required. The feed system pressure vessel is on a movable platform to allow easy transition from one gasifier to the other. An internal mixer allows for the feeding of more difficult materials such as biomass materials to be completed on this system.

During operation of the system, fly ash was captured in a HGFV that uses an iron aluminide candle filter, providing near-absolute filtration. The gas then passed through water–gas shift reactors that can shift sour gas (containing H_2S) to increase its H_2 concentration. The gas then passed through water quench pots to remove tars and a portion of the H_2S. A portion of this gas was then sent to a piece of technology that was the reason for the tests, and the rest was combusted in the thermal oxidizer from which the M29 and M26A samples were collected. Approximately 85% of the 2500 ppm of H_2S in the gas was removed with a zinc-based fixed-bed sorbent system before the thermal oxidizer. The gas that was passed through the special equipment being tested during this run was flared separately.

The FBG operates at lower temperatures than the EFG. As a result, more CH_4 is produced by the FBG. Hydrogen concentration in the dry gas resided in the 40% range during the tests. CO was in the 2.5% range, while CO_2 was in the low-50% range in the dry gas. The high CO_2 concentration indicated that the sour gas shift catalysts were operating correctly. CH_4 typically runs at about 3%. Hydrocarbons and trace organics may also be produced by the FBG. These are largely dependent on fuel type and operational parameters. The N_2 purge requirements of the FBG are substantially lower than for the EFG, resulting in much lower N_2 dilution of approximately 3% of the dry gas.

The microcontaminant sampling consisted of collecting particulate- and vapor-phase elements using two sampling trains, one designed for EPA M26A halogen sampling and the other designed for EPA M29 trace metals sampling. The thermal oxidizer contains a burner at the top of a refractory-lined chamber that admits the syngas and air separately and also includes a premixed natural gas and air supplemental gas stream. An accurate flame temperature is not available for the thermal oxidizer because thermocouples burn out too quickly in the flame. The sampling occurs at the bottom of the downfired oxidizer. The gas being sampled is at approximately 750°C. It is quenched as it is pulled through the glass sampling tube to approximately 100°C before reaching the filter. The sampling train consists of a one-piece glass nozzle/probe liner, a large particulate cyclone, the polycarbonate filter (Whatman™ Nuclepore™ type with a melting temperature of 250°C), followed by a series of impingers (five for M26A and six for M29), shown in Figure 9. Impingers are of a standard Greenburg–Smith design type and are connected in series with leak-free ground brass fittings.

In M29, the first and second impingers contain 150 mL each of the mixture HNO_3–H_2O_2 (5% HNO_3 and 10% H_2O_2), the third impinger is empty, the fourth and fifth impingers both contain 150 mL of the mixture H_2SO_4–$KMnO_4$ (4% $KMnO_4$ and 10% H_2SO_4), and the sixth impinger contains about 350 g of preweighed silica gel. The mixture HNO_3–H_2O_2 is used to trap all the heavy and trace metals (including the oxidized form of mercury) which have gone through the filter's pores, while the H_2SO_4–$KMnO_4$ mixture is used to trap the elemental form of mercury.

In M26A, the first and second impingers each contain 100 mL of 0.1 N H_2SO_4. The third and fourth impingers contain 100 mL of 0.1 N NaOH. The fifth impinger contains about 350 g of silica gel. The H_2SO_4 solution is used to solubilize hydrogen halides that have been vaporized to the gas phase, while the NaOH solution is used to hydrolyze halogens (Cl_2, Br_2) into protons (H+), halide ions, and hypohalous acids (HClO and HBrO). Then Na_2SO_4 is added to the alkaline solution to assure reaction with the hypohalous acid to form a second halide ion such that two halide ions are formed for each molecule of halogen gas. Before sampling, a pretest leak check is conducted, and the initial meter volume is recorded. For each run, the required data are recorded on a data sheet. At the end, the glassware is disconnected and the contents of the acid impingers are poured into a leak-free storage bottle. Each impinger is rinsed with water, and the rinse is added to the corresponding storage bottle. All sample collection bottles are sealed, labeled, and sent to the analytical lab for analysis.

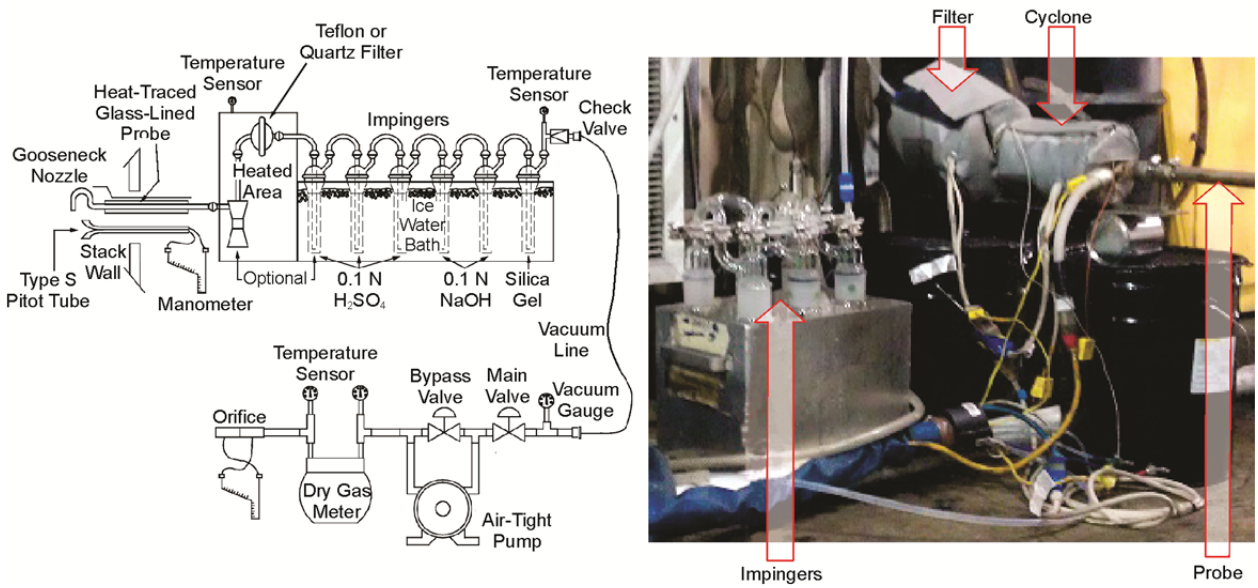

Figure 9. M29 and 26A sampling train.

M26A is applicable for the determination of hydrogen halide (HCl, HBr, and HF) and halogen (Cl_2 and Br_2) emissions from stationary sources. The impinger solutions are analyzed by ion chromatography (IC), which detects and quantifies the amount of F^-, Cl^-, and Br^- ions in these solutions. The concentration of a target hydrogen halide or halogen emission in solution is suggested to be greater than the corresponding lower limit of quantification (LLQ) to be detected by the IC system. The minimum detection limit for bromide, chloride, and fluoride is 1 mg/L, using the EERC equipment for M26A.

M29 is applicable to the determination of EPA-designated hazardous metal emissions such as lead (Pb), nickel (Ni), manganese (Mn), mercury (Hg), selenium (Se), cadmium (Cd), chromium (Cr), silver (Ag), thallium (Tl), arsenic (As), antimony (Sb), barium (Ba), beryllium (Be), cobalt (Co), phosphorus (P), zinc (Zn), and copper (Cu) from stationary sources. However, in the future we will also analyze the solutions for major elements. A stack sample is withdrawn isokinetically from the source, particulate emissions are collected in the probe and on a heated filter, and gaseous emissions are then collected in aqueous acidic solutions of H_2O_2 and $KMnO_4$, respectively. While filters are analyzed using scanning electron microscopy (SEM), impinger solutions are analyzed using different spectroscopic techniques such as cold-vapor atomic absorption spectrometry (CVAAS) for Hg and inductively coupled plasma–mass spectrometry (ICP–MS) for the remaining trace metals. A target trace metal emission will be detected if and only if its concentration is above the corresponding LLQ. The LLQ for the trace metals analyzed in this work are presented in Table 1. Although the impinger solutions have so far only been analyzed for trace metals using a standard analysis matrix, in the near future they will also be analyzed for major elements.

Table 1. Limit of Detection of Trace Metals Analyzed

Trace Metal:	As	Be	Cd	Co	Cr	Mn	Ni	Pb	Sb	Se
LLQ, µg/L	0.5	0.1	0.1	0.5	0.1	0.1	0.2	0.1	0.1	1.0

The data that have been reduced to report form are for a sampling period from March 2012 to April 2012. The March samples were collected from the EFG during testing described in the January to March quarterly technical progress report. The April samples were collected during a test with the FBG as described in the April to June quarterly report. Samples were collected on March 27 (blank – natural gas only), March 28 (syngas), March 30 (blank – natural gas only), April 11 (syngas), and April 18 (syngas), 2012 respectively. Rust was found on the filter for the March 27 sampling so that sample has been rejected for data analysis. The source of the rust was found and cleaned before the next sampling date. The filter melted during the March 28 sampling, and most of the solid particles went into the impinger solutions, but the filter will still be analyzed by SEM to determine what portion of the impinger species were likely present as particulate matter.

RESULTS AND DISCUSSION

Laboratory Testing and Modeling

Figures 10–13 show SEM images of diffusion-bonded samples. The images have been overlaid with energy-dispersive spectroscopy (EDS) results showing the distribution of Zn throughout the joints. Figure 10a shows the zinc distribution in a joint of CM247LC after 1 hour at 1214°C. The image was taken near the outer edge of the joint. It clearly shows an increase in the Zn concentration as one moves from the outside of the joint (right side of image) toward the inner portion of the joint (left side of image). This indicates that some of the zinc has already diffused out of the joint and evaporated in as little as 1 hour. Figure 10b shows a region near the center of the joint, illustrating that the zinc concentration is consistent throughout the middle portion of the sample.

Figure 11 shows the EDS overlay on a SEM image for a CM247LC joint after 3 hours at 1214°C taken at the center of the joint. Zn remains in the sample, but there has been a significant reduction in the concentration when compared to Figure 3b.

Figure 12 shows the distribution of zinc in the center of a Rene 80 sample after 1 hour at 1214°C. The zinc distribution is similar in Rene 80 to that seen in CM247LC. In contrast, Figures 13a and 13b show the distribution of zinc in a joint of APMT after 1 hour and 3 hours, respectively. Comparing these results with Figures 10–12, it is apparent that the diffusivity of zinc in APMT is much higher than in CM247LC or in Rene 80.

Perhaps the most interesting feature of Figures 10–13 is not what is present in the joints, but what appears to be missing – grain boundary diffusion. Reviews of previous work related to zinc diffusion indicated that grain boundary diffusion was likely to be observed under the current conditions. The fact that the motion of the Zn instead appears to be by bulk diffusion is

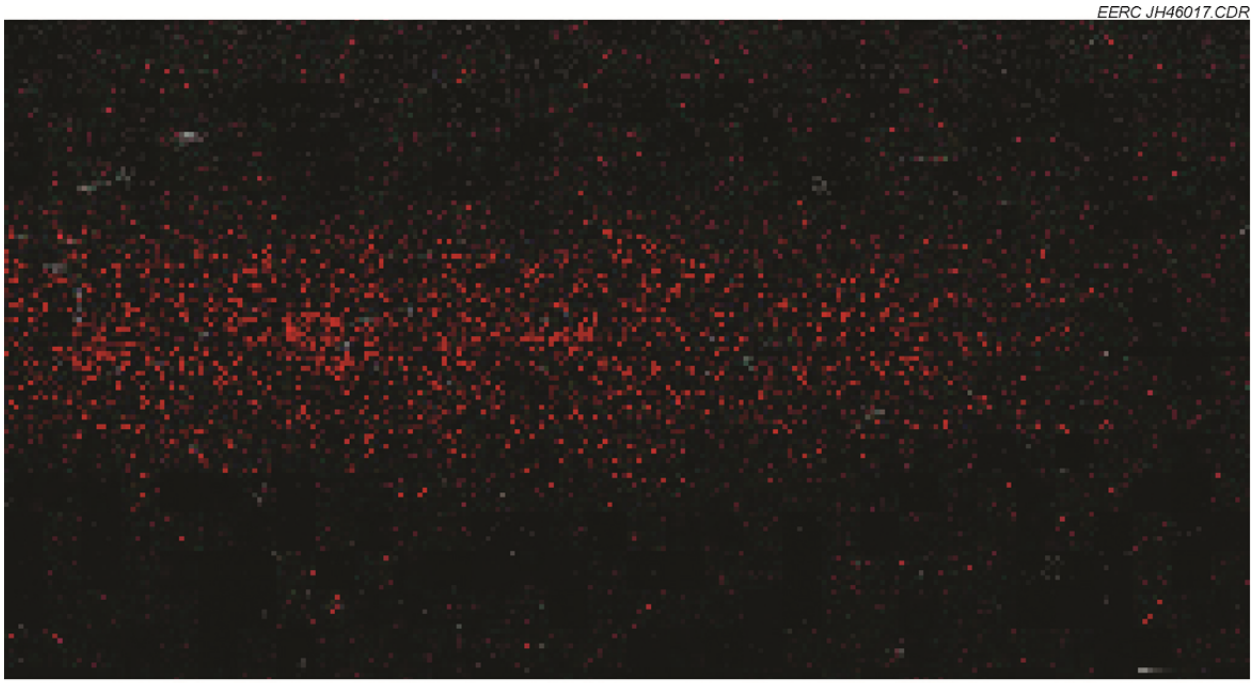

(a)

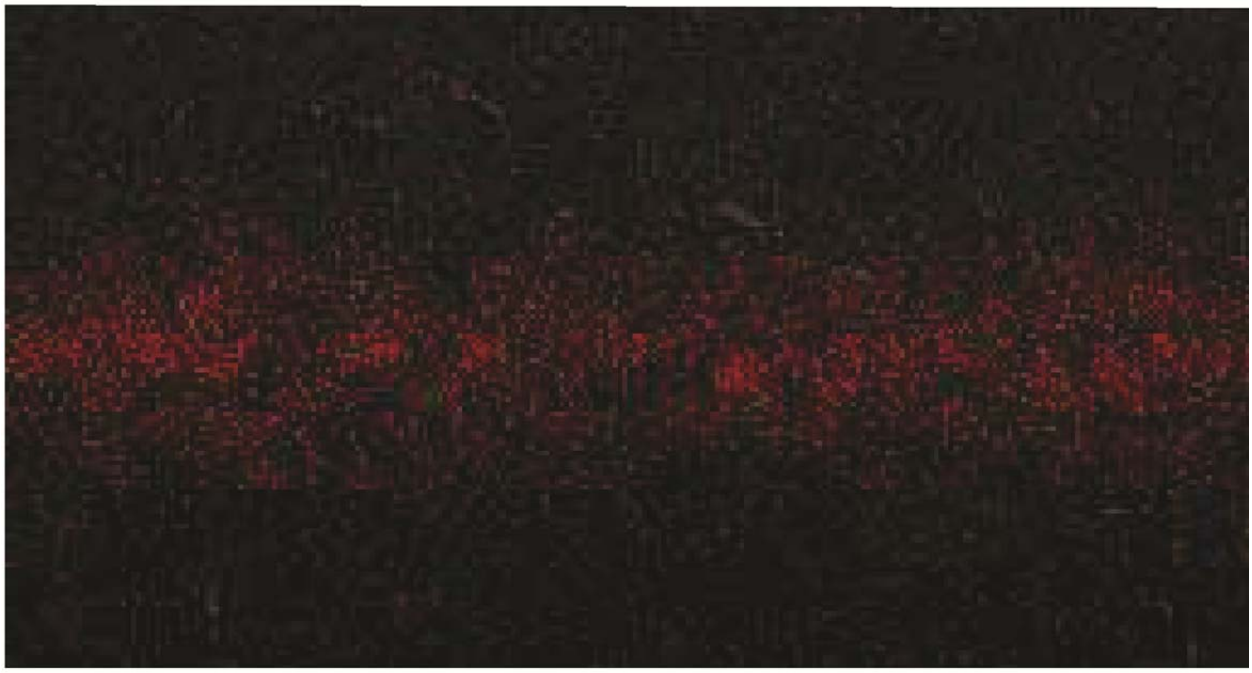

(b)

Figure 10. Elemental map of Zn – CM247LC bonded at 1214°C for 1 hour: a) joint edge and b) joint center.

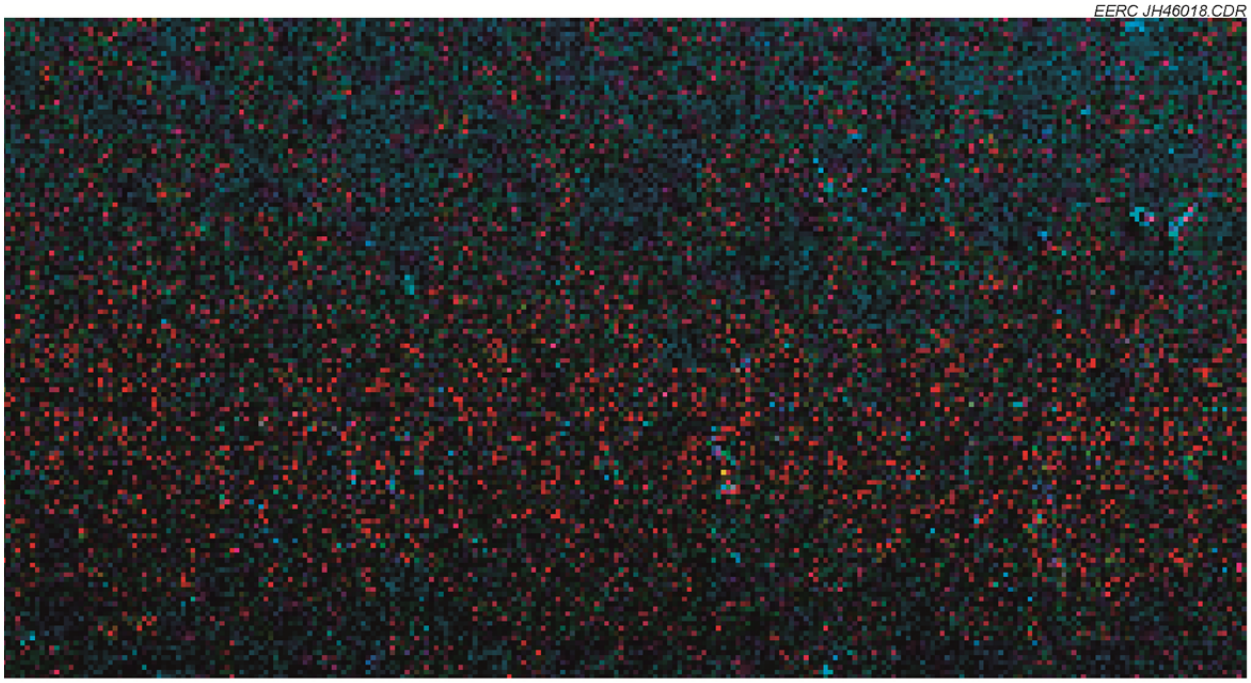

Figure 11. Elemental map of Zn – CM247LC bonded at 1214°C for 3 hours (joint center).

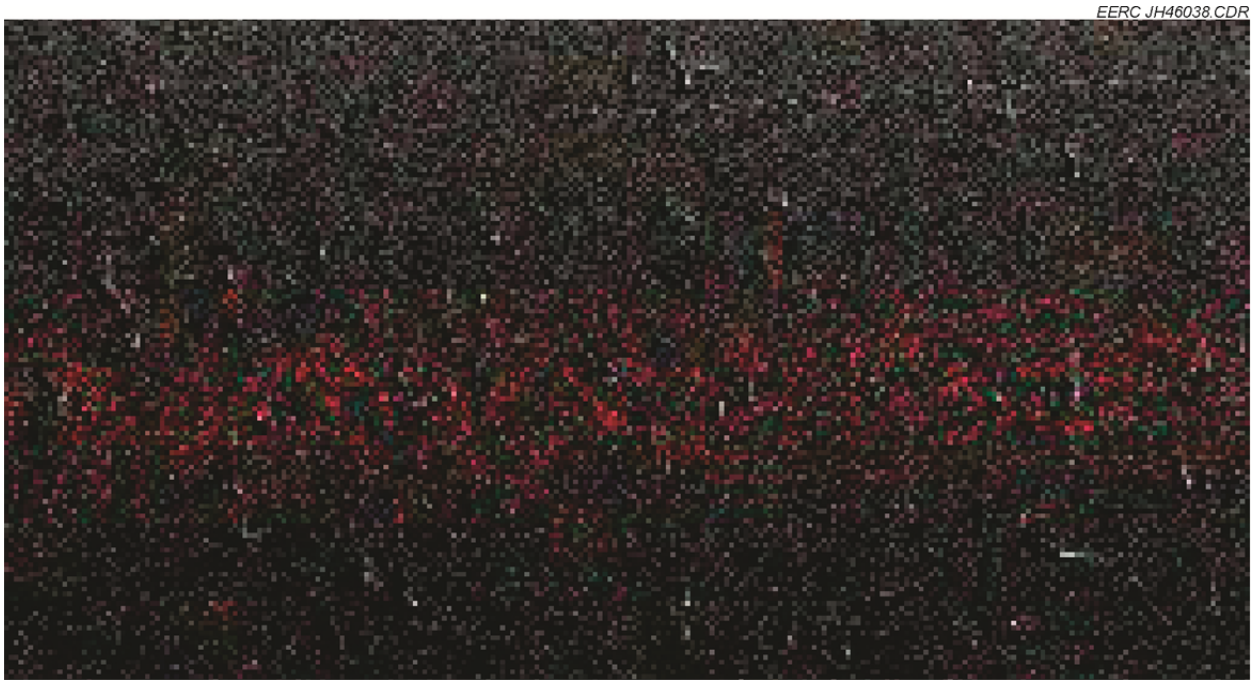

Figure 12. Elemental map of Zn – Rene 80 bonded at 1214°C for 1 hour (joint center).

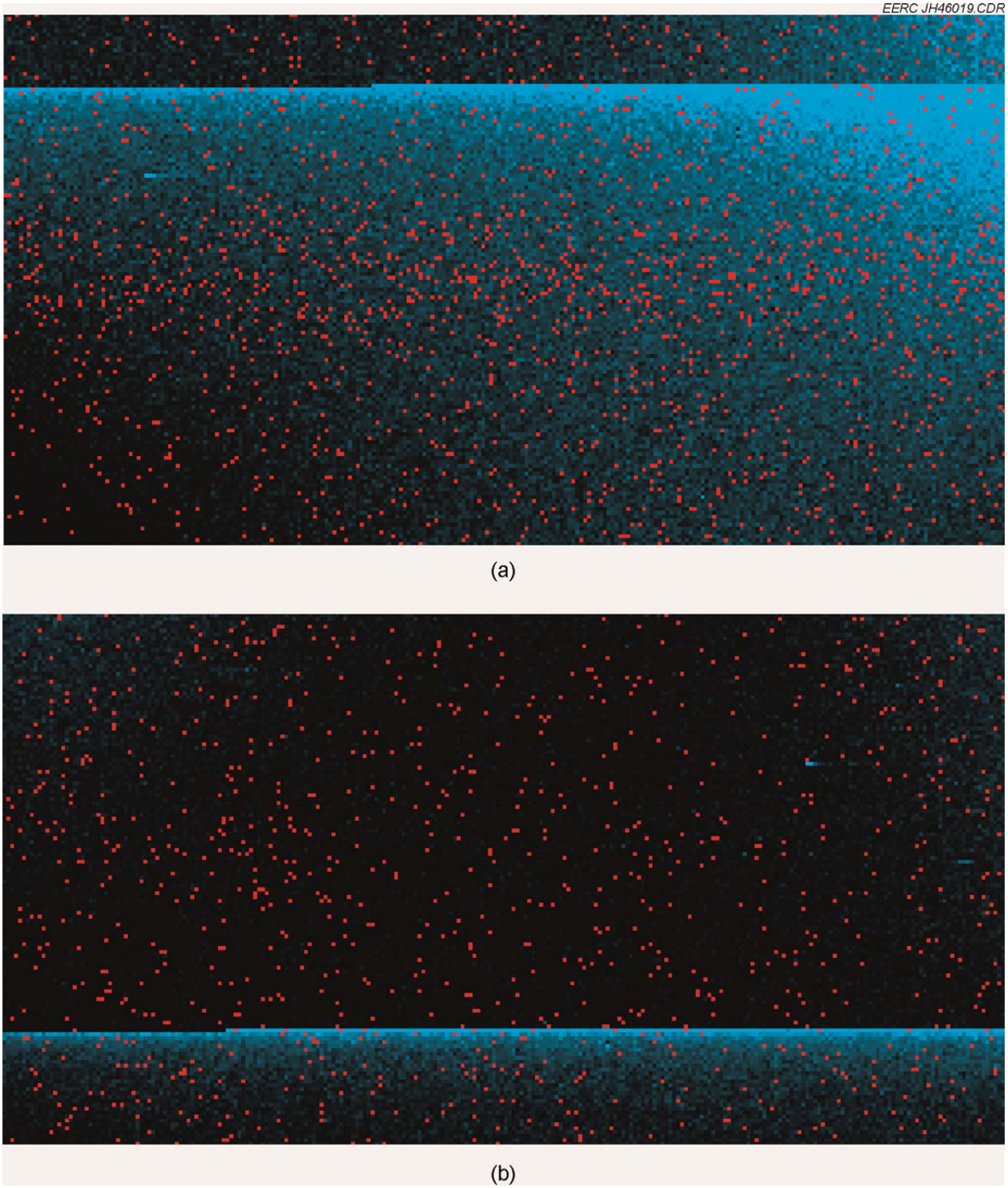

Figure 13. Elemental map of Zn – APMT bonded at 1214°C (joint center) for a) 1 hour and b) 3 hours.

surprising. However, these results mean that quantification of the Zn diffusivities in these samples will be significantly simpler than would have been the case if grain boundary diffusion dominated. Quantitative Zn diffusion profiles are currently being generated for the samples so that diffusivities can be calculated and the complete history of the Zn from bonding foil to diffusion through the alloys to evaporation can be understood.

In tandem with the experimental diffusion-bonding work, a numerical model of the bonding assembly has been constructed. Figure 14 shows finite element analysis results using the numerical model for two applied loading conditions. In Figure 14a, the loads are applied via an applied pressure at the bond line. In Figure 14b, the loads are applied via an applied pressure at the edge of the steel end cap. The two approaches result in similar strain distributions within the joint itself but some differences in strains in the jig. These results were obtained using generic material properties for the materials in the bonding assembly. Preliminary data have been gathered for the actual material properties for both the jig materials and the bonding samples.

Gasifier Sampling

Impinger Solution Analyses

Analytical results for EPA hazardous emission elements are presented in Tables 2–6 according to their respective sampling dates. In the future, the solutions will be analyzed for major elements. The concentration of each element is given for the solution analyzed and for the gas volume that was sampled. In these tables, the nozzle results are absent because no nozzle was used in this work. Any value below the element's LLQ is classified as nondetected and shaded in gray. The values highlighted in green are classified as detected values since they are above the element's LLQ and were well-quantified. The oxidized form of Hg is shown in the H_2O_2 solution, while its elemental form is shown in the $KMnO_4$ solution.

The data show that when only natural gas is fired, as in Test 3, all of the hazardous elements analyzed for the M29 test matrix except As and Co are present in the gas collected from the thermal oxidizer. It is not yet known if the metals come into the thermal oxidizer in the natural gas or air or, more likely, are contaminants previously deposited in the thermal oxidizer. However, when syngas is fired, as in Test 4, the amount of Mn in the gas stream increases substantially. A comparison between the Test 2 and Test 4 results shows much higher Ni and Cr in solution in Test 2, indicating that either the EFG produces more of those elements in the syngas than when using the FBG or that those elements are in the particulate matter that would normally be collected by the filter but were not separated in Test 2 because the filter had failed. IC results show that halogens (Br_2 and Cl_2) and hydrogen halides (HF, HCl, and HBr) in amounts close to or below their respective LLQ of 1 ppm. This might be because all the M26A samples were collected from the outlet of a FBG. In the near future, more M26A samples will be collected during EFG testing to determine if their levels remain low. In addition, in the future, the solutions will be reanalyzed for major elements.

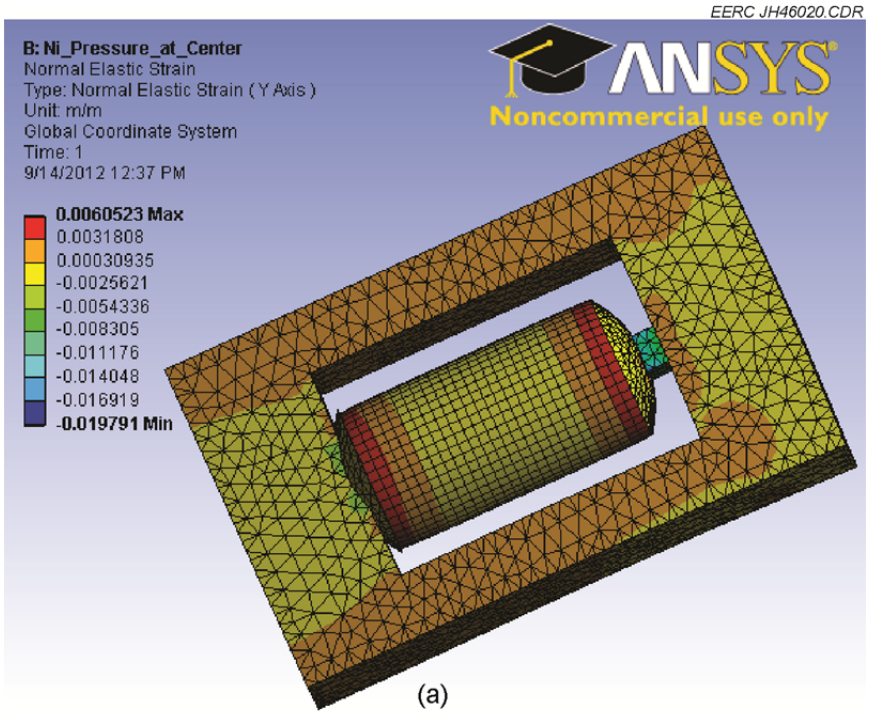

(a)

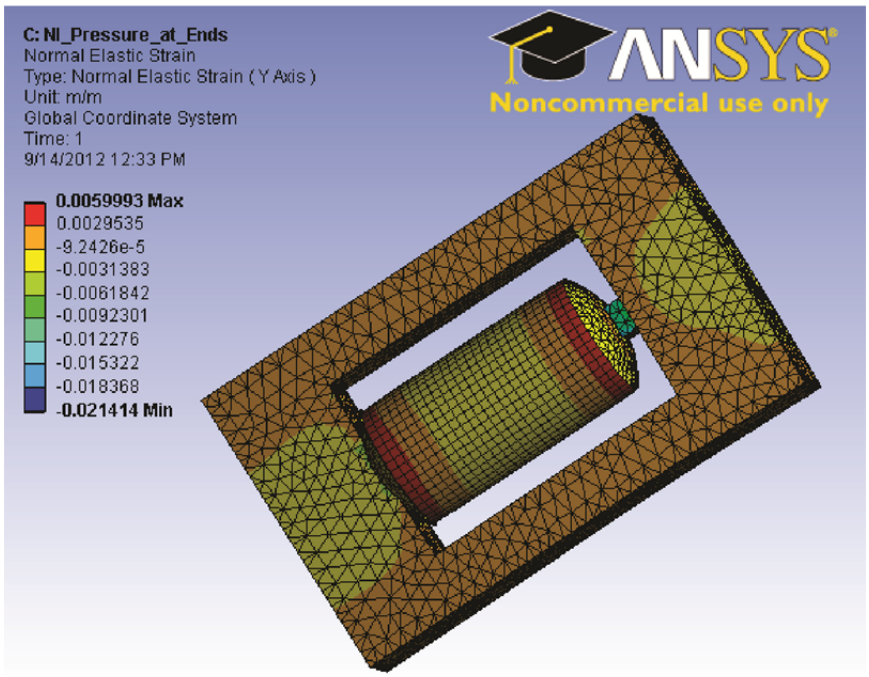

(b)

Figure 14. Comparison of strains in the bonding assembly when loads applied at a) joint center or b) joint ends.

Table 2. M29 Results, Test 2, March 28, 2012 (EFG firing Montana subbituminous Rosebud + torrefied wood but with melted filter)

Date: 3/28/2012
Sample I.D.: EFG-039-M29
Test Length: 150 min
VmSTD, ft^3: 43.666

		As	Pb	Hg	Sb	Ni	Mn	Se	Be	Cd	Co	Cr
	LLQ, µg/L	0.50	0.10	0.02	1.00	0.20	0.10	1.00	0.10	0.10	0.50	0.10
H_2O_2	Conc., µg/L	0.40	1.90	0.15	2.00	58.70	20.80	0.40	0.20	18.80	0.44	48.60
	Conc., µg/m^3	0.16	0.77	0.06	0.81	23.75	8.42	0.16	0.08	7.61	0.18	19.66
$KMnO_4$	Conc., µg/L			3.550								
	Conc., µg/m^3			1.44								

Note: Data not corrected for O_2 (dry basis).
Shaded values are below LLQ.

Table 3. M29 Results, Test 3, March 30, 2012 (no syngas, natural gas firing only)

Date: 3/30/2012
Sample I.D.: EFG-039-3-30-12-M29
Test Length: 217 min
VmSTD, ft^3: 63.684

		As	Pb	Hg	Sb	Ni	Mn	Se	Be	Cd	Co	Cr
	LLQ, µg/L	0.50	0.10	0.02	1.00	0.20	0.10	1.00	0.10	0.10	0.50	0.10
H_2O_2	Conc., µg/L	0.40	1.20	0.13	0.00	12.80	13.30	2.20	0.20	0.20	0.40	9.82
	Conc., µg/m^3	0.11	0.33	0.04	0.00	3.55	3.69	0.61	0.06	0.06	0.11	2.72
$KMnO_4$	Conc., µg/L			0.138								
	Conc., µg/m^3			0.04								

Note: Data not corrected for O_2 (dry basis).
Shaded values are below LLQ.

Table 4. M29 Results, Test 4, April 11, 2012 (FBG firing the Montana subbituminous Rosebud coal)

Date: 4/11/2012
Sample I.D.: FBG-025-4-11-12-M29
Test Length: 223 min
VmSTD, ft^3: 60.681

		As	Pb	Hg	Sb	Ni	Mn	Se	Be	Cd	Co	Cr
	LLQ, µg/L	0.50	0.10	0.02	1.00	0.20	0.10	1.00	0.10	0.10	0.50	0.10
H_2O_2	Conc., µg/L	0.40	0.76	0.16	0.00	7.53	63.80	1.10	0.20	0.20	0.40	8.20
	Conc., µg/m^3	0.12	0.22	0.05	0.00	2.19	18.58	0.32	0.06	0.06	0.12	2.39
$KMnO_4$	Conc., µg/L			0.839								
	Conc., µg/m^3			0.29								

Note: Data not corrected for O_2 (dry basis).
Shaded values are below LLQ.

Table 5. M26A Results, Test 5, April 11, 2012 (FBG firing the Montana subbituminous Rosebud coal)

Date: 4/11/2012
Sample I.D.: FBG-025-4-11-12-M26
Test Length: 60 min
VmSTD, ft^3: 9.198
LLQ: 1 mg/L

	Chloride, ppm	Fluoride, ppm	Bromide, ppm
H_2SO_4 in Flue Gas	1.30	2.30	0.60
NaOH in Flue Gas	0.00	0.00	0.00
Total, µg/m^3	1.30	2.30	0.60

Table 6. M26A Results, Test 6, April 18, 2012 (FBG firing the Montana subbituminous Rosebud coal)

Date: 4/18/2012
Sample I.D.: FBG-025-4-18-12-M26
Test Length: 150 min
VmSTD, ft^3: 40.294
LLQ: 1 mg/L

	Chloride, ppm	Fluoride, ppm	Bromide, ppm
H_2SO_4 in Flue Gas	0.30	0.50	0.10
NaOH in Flue Gas	0.00	0.00	0.00
Total, $\mu g/m^3$	0.30	0.50	0.10

SEM Analysis of a Filter Sample

During this quarter, the particles captured on the filter from the M29 test performed on April 11 were analyzed by SEM in a preliminary determination of the types and sizes of particles captured. Filter samples were first kept in a desiccator (Figure 15) and later analyzed using the EERC JEOL 5800 SEM equipped with Oxford Instruments INCA EDS system and a silicon drift x-ray detector.

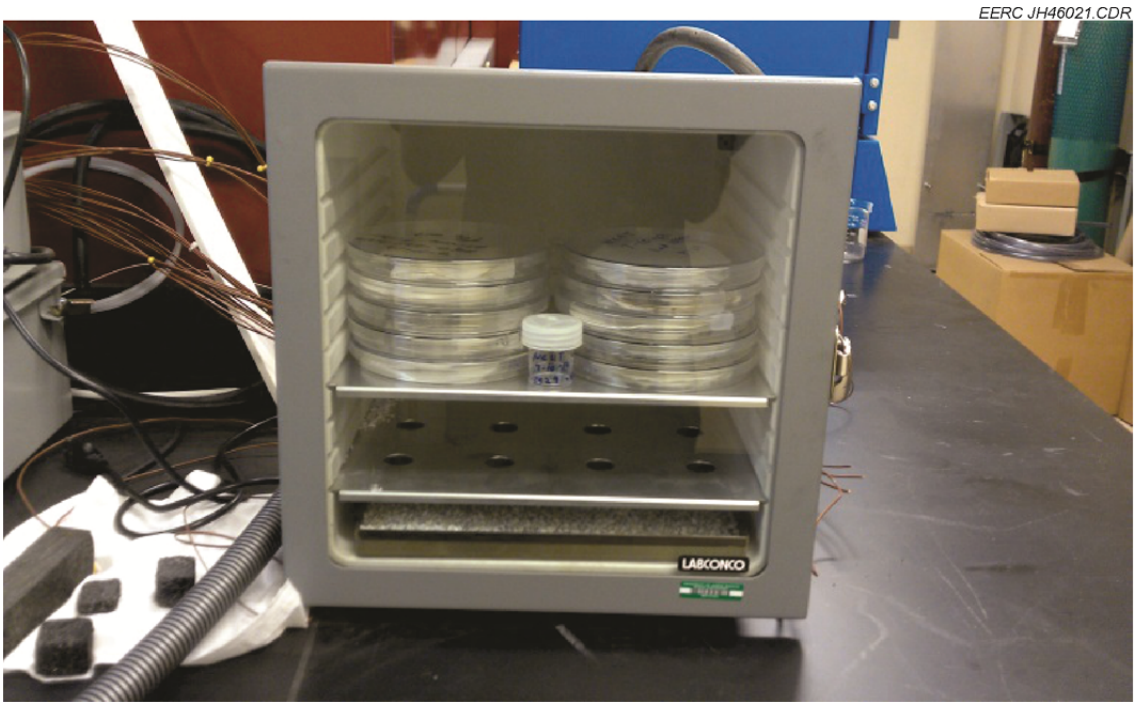

Figure 15. Desiccator containing collected filter samples.

A total of 3089 particles were analyzed and spectra acquired for 20s using a 2-nA beam current at 20-kV accelerating voltage. Elements such as Fe, S, Cr, Si, and some traces of Na, Mg, Al, K, Mn, and Ni were mainly found on the filter surface. Figure 16 shows SEM images of the filter at different magnifications.

To characterize filter particles, five-spot (particles) were chosen at random on the filter surface (Figure 17) and underwent a full spectral analysis.

The compositions of the five particles are shown in Table 7.

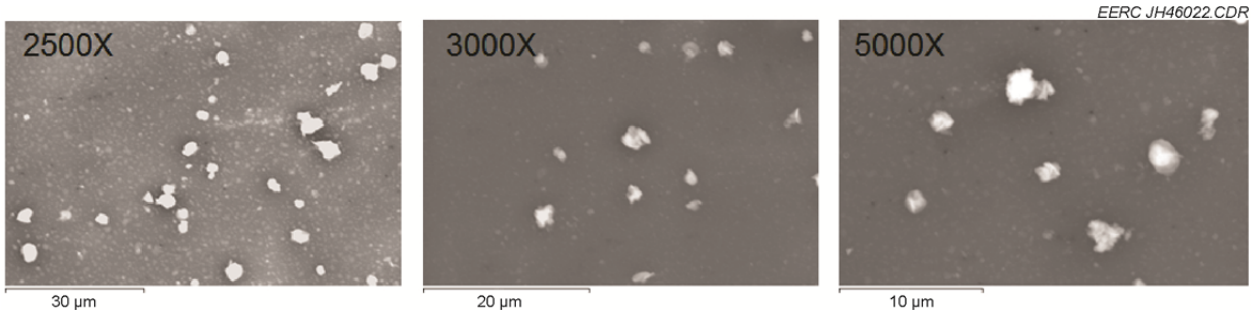

Figure 16. SEM images of the filter particles obtained at different magnifications.

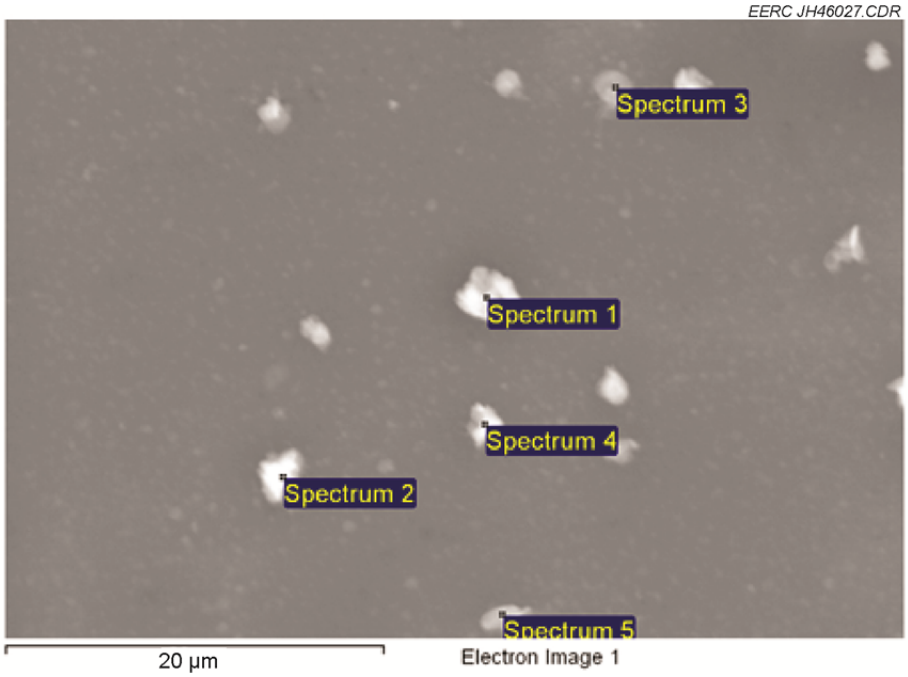

Figure 17. Particles chosen for full spectral analysis.

Table 7. Elemental Compositions of the Five Particles Chosen

	O	Si	S	Cr	Fe	Ni	Total
Particle 1	63.8	3.7	19.0	2.1	11.4		100.0
Particle 2	62.7	2.7	19.4	2.0	12.1	1.1	100.0
Particle 3	70.3		17.3		12.5		100.0
Particle 4	65.5	3.3	18.1	2.5	10.6		100.0
Particle 5	72.5		17.1		10.4		100.0
Max.	72.5	3.7	19.4	2.5	12.5	1.1	
Min.	62.6	2.7	17.1	2.0	10.4	1.1	

Figure 18 shows the cumulative size distributions of the 3089 particles analyzed. Most of the particles were 3 µm in diameter or less. Elements such as O, Fe, S, Cr, Si, and traces of Na, Ni, Al, Mg, K, Ca, and Mn were detected in the 3089 particles on the filter surface. The concentrations of O and S were high in almost all particles. The elemental concentrations as functions of size are shown in Figure 19. The data show that the concentrations of sulfur and iron tend to be higher in the larger particles than in the smaller. In contrast, the concentrations of O showed the reverse trend. The average shape factor of most particles was about 1.2, as shown in Figure 20, which also shows that there was little correlation between composition and shape. A shape factor of 1.2 means that most of them have a nearly spherical shape.

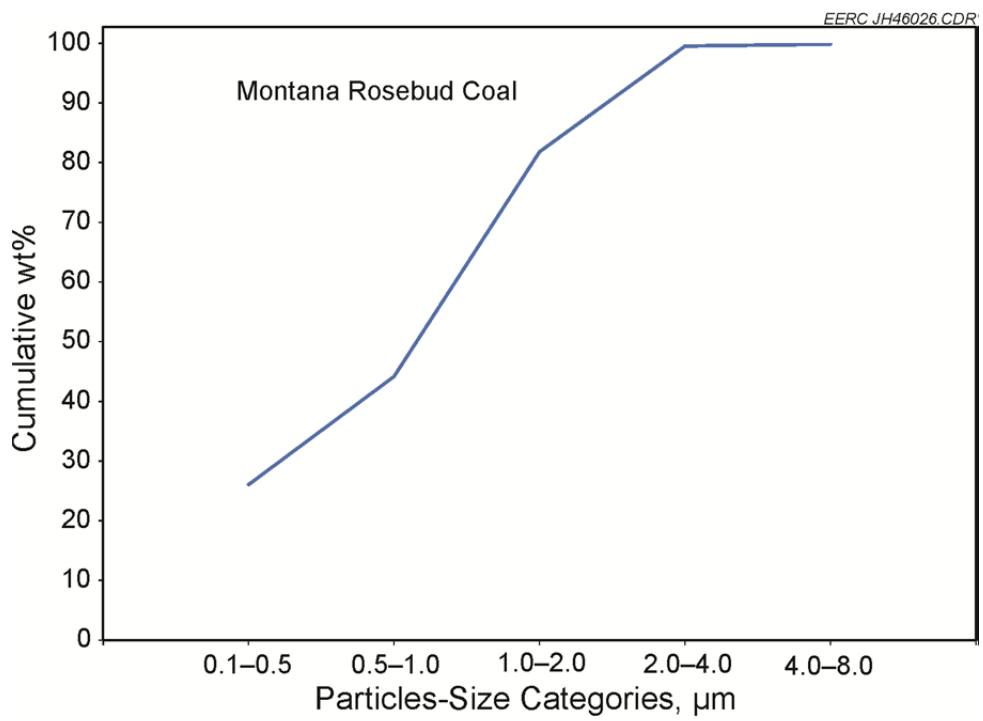

Figure 18. Cumulative size distribution of the 3089 particles analyzed.

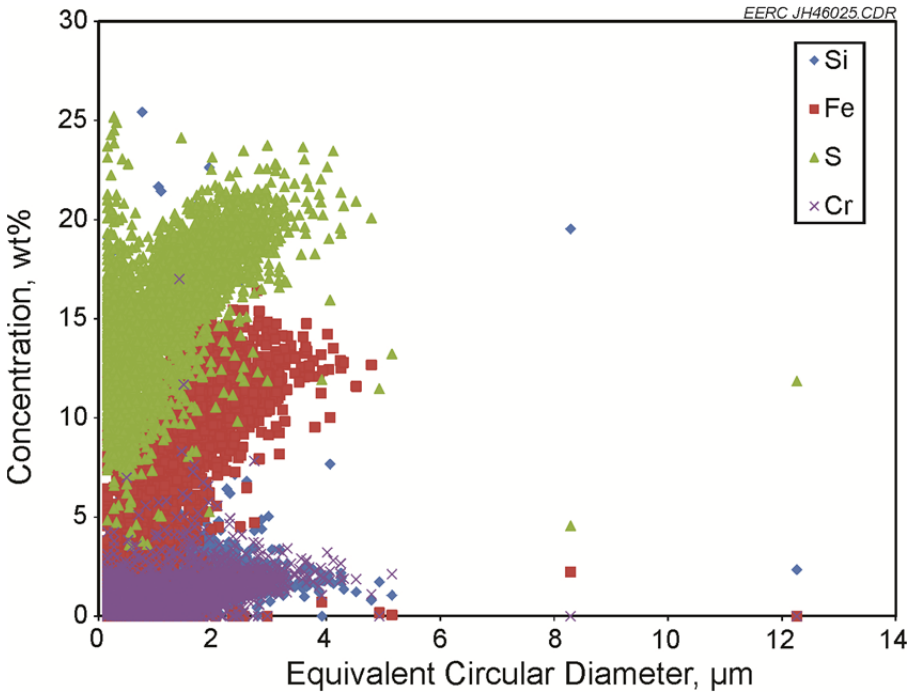

Figure 19. Composition vs. size of particles.

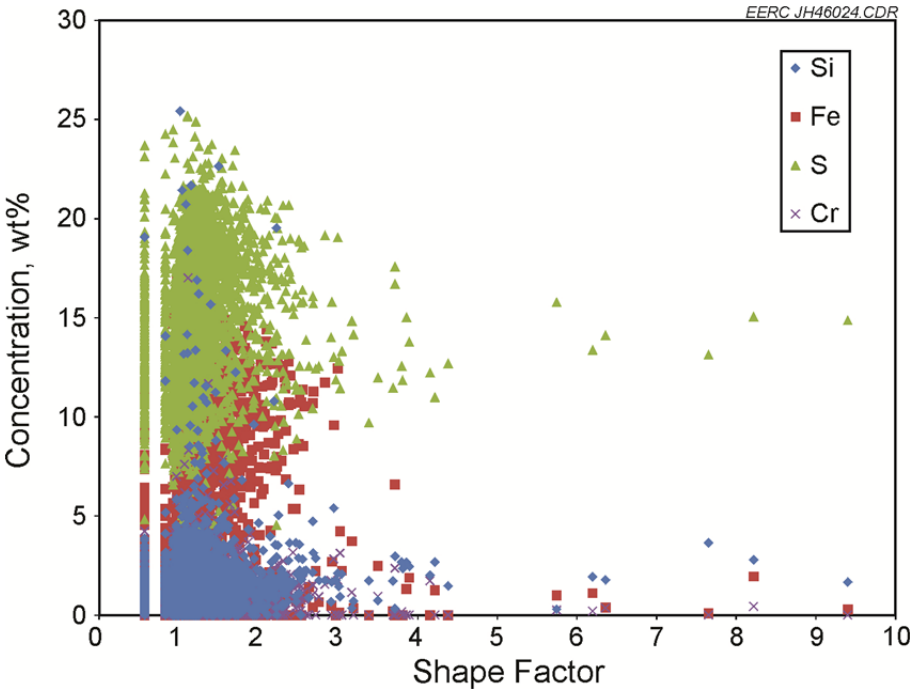

Figure 20. Composition vs. shape of particles.

We currently believe that the high values of Fe and Cr observed on the filter samples come from a reaction of the syngas with the stainless steel pipes used to transport the syngas, most likely by forming a vapor-phase carbonyl. The composition of 316L stainless steel is shown in Table 8. During combustion of the carbonyls in the thermal oxidizer, they react to form nonstoichiometric sulfate particles. The excess Si is most likely coming from the coal ash, possibly through the formation of a silicon monoxide fume. In the thermal oxidizer, the silicon monoxide may oxidize to form a small particle of silicon dioxide which may then serve as a nucleation site for the iron-rich sulfate.

CONCLUSIONS

Laboratory testing has shown that the diffusion rate of Zn through the FeCrAl alloy is much faster than through the nickel superalloys. This means that the FeCrAl will serve as a sink for the Zn during the EMB process. Also, the testing has shown that the Zn diffusion mechanism is bulk diffusion, and not intergranular. This is a surprise. However, it means that quantification of the Zn diffusivities in these samples will be significantly simpler than would have been the case if grain boundary diffusion dominated. Quantitative Zn diffusion profiles are currently being generated for the samples so that diffusivities can be calculated and the complete history of the Zn from bonding foil to diffusion through the alloys to evaporation can be understood.

In addition to the laboratory testing, gas impinger and particulate samples are being collected from a combustor firing syngas and natural gas to determine what type of microcontaminants may reach a turbine system firing syngas. The syngas is created in one of two different pilot-scale pressurized gasifiers. The initial analysis of the impinger solutions was for standard EPA M29 determination of hazardous metals. The data show that when only natural gas is fired in the combustor, all of the hazardous elements analyzed for the M29 test matrix except As and Co are present at low levels in the gas collected from the thermal oxidizer. It is not yet known if the metals come into the thermal oxidizer in the natural gas or air or, more likely, are contaminants previously deposited in the thermal oxidizer. However, when syngas is fired, the amount of Mn in the combustor gas increases substantially. IC results show that halogens (Br_2 and Cl_2) and hydrogen halides (HF, HCl and HBr) are present in amounts close to or below their respective LLQ of 1 ppm. In the near future, more M26A samples will be collected during EFG testing to determine if their levels remain as low as for the FBG samples. In addition, the solutions will be reanalyzed for major elements.

SEM analysis showed that the particulate matter is primarily nonstoichiometric iron sulfate. Most of the particles were 3 µm in diameter or less. Elements such as O, Fe, S, Cr, Si, and traces of Na, Ni, Al, Mg, K, Ca, and Mn were detected in the 3089 particles analyzed on the

Table 8. Composition of 316L Stainless Steel, wt% (max.)

Element	C	P	S	Cr	Ni	Mo	Mn	Si	Fe
	<0.03	<0.045	<0.03	16–18	10–14	2–3	<2	0.75	Balance

filter surface. The concentrations of O and S are high in almost all particles. The data show that the concentrations of sulfur and iron tend to be higher in the larger particles than in the smaller. In contrast, the concentrations of oxygen showed the reverse trend. The average shape factor of most particles was about 1.2, meaning that most of them have a nearly spherical shape.

We currently believe that the high values of Fe and Cr observed on the filter samples come from a reaction of the syngas with the stainless steel pipes used to transport the syngas, most likely by forming a vapor-phase carbonyl. During combustion of the carbonyls the metals react with S and O to form nonstoichiometric sulfate particles. The excess Si is most likely coming from the coal ash, possibly through the formation of a silicon monoxide fume. In the thermal oxidizer, the silicon monoxide may oxidize to form a small particle of silicon dioxide, which may then serve as a nucleation site for the iron-rich sulfate.